Optimized retrieval of 1D-resistivity profiles in cover concrete by electrical sounding measurements

Yannick Fargier, Géraldine Villain, Sérgio Palma Lopes, Milia Fares

Optimized Retrieval of 1D-resistivity profiles in cover concrete by electrical sounding measurements

Yannick Fargier(1*), Géraldine Villain(2), Sérgio Palma Lopes(2), Milia Fares(2,3)

(1) Université Gustave Eiffel, Campus de Bron, 25 avenue François Mitterrand, CS24, 69675 Bron cedex, France

(2) Université Gustave Eiffel, Campus de Nantes, Allée des Ponts et Chaussées, CS 5004, 44 344 Bouguenais cedex, France

(3) BTP Consultants, 460 Boulevard du Mont d'Est, 93160 Noisy-le-Grand

* Corresponding author: yannick.fargier@univ-eiffel.fr

Abstract: Geophysical techniques offer assessing conditions of reinforced concrete structures without invasiveness issues. Electrical Resistivity methods are promising tools for evaluating parameters such as water and ionic contents of concrete in reinforced concrete structures. In order to obtain water content profiles due to water ingress, the actual challenge consists in evaluating the *1D*-resistivity profile with depth in concrete. To reach this goal, *1D*-inversion procedures improving the extraction of true resistivity profiles in concrete are proposed. The first procedure, considered more conventional, is based on a discrete parameterization of the medium with three parameters. The second procedure is based on a continuous parameterization function defined with four parameters. We invert synthetic profiles to test the procedures and we study the effect of data noise on the inversion results. At last, an experimental validation on concrete slabs is carried out by comparing four different saturation degree profiles extracted from measurements or obtained by reference measurements. Results show that the continuous parameterization is able to accurately retrieve several profiles but that the resolution of the resistivity profile is limited by the maximum inter electrode spacing.

Keywords : electrical resistivity; finite element method; inversion; concrete; water content;

Short Title : *1D* resistivity profiles retrieval in cover concrete

Highlights:

1) We propose a discrete and a continuous *1D* parameterization of the inverse problem

2) A numerical and a sensitivity study are performed to evaluate the two parametrizations

3) True resistivity profiles vs. depth are retrieved from experimental data

4) Retrieved *1D* resistivity profiles are consistent with gammadensimetry results

1 Introduction

Concrete is a construction material of high economic interest worldwide. The initiation of steel reinforcement corrosion, a major reinforced concrete (RC) issue, is related to the ingress of aggressive agents, including water and chlorides (Baroghel-Bouny et al., 2007; Bentur et al., 1997) . Therefore, the early and cost-effective detection of water and chloride ingress into cover concrete is important and the determination of water and chloride content profiles is an even more important challenge for durability diagnosis of RC structures and prognosis of their servicelife (Baroghel-Bouny et al., 2007).

Geophysical or Non-destructive evaluation (NDE) techniques significantly contribute to concrete condition assessment (Balayssac et al., 2015) and therefore to reinforced concrete structure maintenance. It is now well established that electro-magnetic (EM) NDE techniques are powerful tools in this context, due to their significant sensitivity to both water and ionic contents (Dérobert et al., 2008; Hugenschmidt and Loser, 2007; Kwon et al., 2010). Recently, research works have addressed the need to estimate water content and chloride profiles by developing specific EM NDE approaches (du Plooy et al., 2015; Fares et al., 2016; Ihamouten et al., 2011).

The present paper focuses on the electrical resistivity measurement method (Monfore, 1968; Whittington et al., 1981; Woelfl and Lauer, 1979). In cover concrete, resistivity depends on the concrete formulation, age, porosity (Karhunen et al., 2010; Whittington et al., 1981) and on its water content or saturation degree (Archie, 1942; Woelfl and Lauer, 1979). These indicators can be assessed using calibration tools (du Plooy et al., 2013; Villain et al., 2018) to give information about the durability of concrete structures (du Plooy et al., 2015; Gowers and Millard, 1999; Lataste et al., 2008; Polder, 2001; Reichling et al., 2015; Sbartai et al., 2007). Vertical Electrical Sounding (VES) approache has been intensively developed in the field of near surface geophysics for the last three decades (Loke et al., 2013). Data acquisition procedures are based on multielectrode layouts and data processing approaches are based on the inversion of measured data to allow the reconstruction of a ‘true’ resistivity distribution (Loke and Barker, 1996). It should be emphasized that the applications of electrical methods to cover concrete investigation are more recent and still scarce (du Plooy et al., 2015, 2013; Karhunen et al., 2010; Reichling et al., 2015; Villain et al., 2015b).

Concerning inversion, 1D inversion are known to be robust mitigating the unavoidable ‘non-uniqueness’ and so under-determination issues (Tarantola and Valette, 1982). When

addressing the investigation of solute transport in cover concrete, we consider that a *1D* inversion scheme (i.e. estimating 'true' resistivity profiles vs depth in cover concrete) is well adapted, as water ingress mainly occurs in a single direction, perpendicular to the concrete surface (Badr et al., 2019; Fares et al., 2016). Here we benefit from our a priori knowledge on the shape of the *1D* solute ingress processes to better determine the inverse problem (Fares et al., 2016).

The aim of this paper is to evaluate true resistivity *1D*-profile inside concrete from surface apparent resistivity measurements. For this purpose, we implement a *1D* inversion scheme, based on a commonly used smoothness constrained least squares algorithm (Loke and Barker, 1996). Then we test two competing model parameterizations that describe the resistivity profile versus depth: a discrete one that is more frequent in *1D* resistivity inversion (Zohdy, 1989) and a continuous one based on a smooth distribution defined by four parameters (Fares et al., 2016).

The structure of the paper is as follows. First, we briefly introduce the main principles of DC-resistivity measurements. Second, our numerical modelling approach is described, which includes the forward and the inverse problems. Third, we present a numerical study that was specifically designed to test and compare the two model parameterization strategies. Then, inversion results based on real data from an experimental campaign (Villain et al., 2015b) are presented with both our inversion schemes. 'True' resistivity profiles are converted into saturation degree profiles to be compared to gammadensimetry results. Finally, we discuss the main findings and we draw conclusions from our research.

2 Basic principle of geo-electrical methods and inversion methodology

The electrical resistivity ρ (Ω.m), is the capacity of a medium to resist the diffusion of an electrical current. In this study, we measure apparent resistivities ρ_a (Ω.m) on the surface of cover concrete. Where ρ_a is the product of the measured transfer resistance R_t (Ω) and a geometrical factor *gf* (m) (Fargier et al., 2014). The transfer resistance is the ratio of the measured voltage drop *V* (V) between potential electrodes (P1 and P2) and the injected current intensity between the current electrodes (C1 and C2). When the spacing between electrodes increase, the investigated volume increases. Thus, multielectrode devices enable to get several apparent resistivities which involve different volumes. Each apparent resistivitie

ρ_a is an integrative measurement which is an intricate function of the true resistivity distribution of a medium. Consequently, we use inversion techniques to reconstruct the true resistivity profile (ρ^{inv}) of cover concrete (Fig. 1). This iterative process contains three main step : the discretization/parametrization of the inversed model, the forward problem and the inverse problem. To be noted that we use a 3D model to take into account the complete geometry of the studied medium (here a slab) (Badr et al., 2019). As illustrated (Fig. 1), prior information plays a key role on the parametrization and the inverse problem.

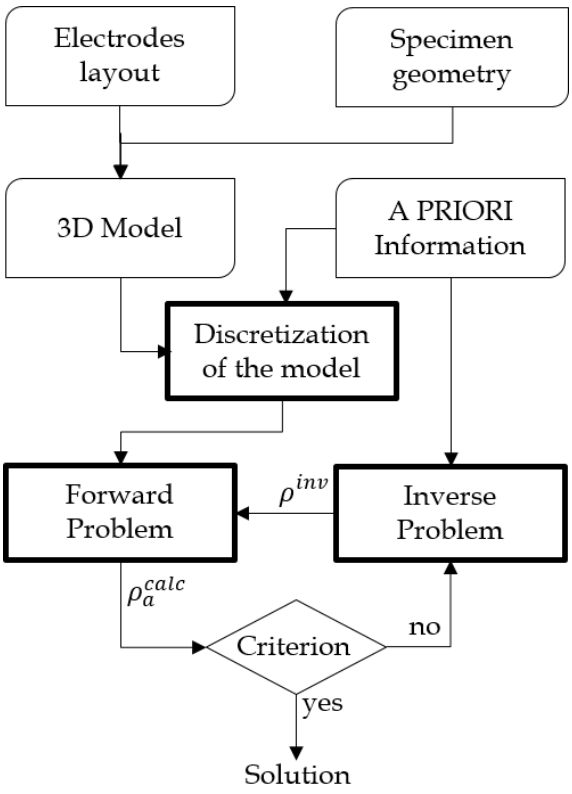

Fig. 1 : Flowchart of the inversion process

2.1 The forward model

The forward problem can be described as follow (Eq. 1):

$$\mathfrak{F}(\boldsymbol{m}) = \boldsymbol{d} \quad \text{(Eq. 1)}$$

Where $\mathfrak{F}$ is the forward problem operator generating data $\boldsymbol{d}$ based on the model $\boldsymbol{m}$. $\boldsymbol{m}$ can be defined as a vector of M parameters continuously or discretely describing the model. The dataset $\boldsymbol{d}$ is composed of N discrete ρ_a measurements. The diffusion of an electrical field in a porous media is governed by Poisson's equation (Eq. 2) representing the forward problem (Rücker et al., 2006).

$$div\left(\frac{1}{\rho}\overrightarrow{grad}(V)\right) = -\sum_{l=1}^{2} I_l\,\delta(r - r_l) \quad \text{(Eq. 2)}$$

Where I (A) is the current intensity injected at a current electrode l located at r_l. Solving this equation can be done by various methods (Günther et al., 2006; Spitzer K., 2007). We use the Finite Element Method (FEM), for its relevance (accuracy and flexibility) for the generation of 3D complex geometries (Fargier et al., 2017; Holcombe and Jiracek, 1984; Pridmore et al., 1981).

2.2 The inverse problem

Conversely, the inverse problem tries to find the physical properties of a medium that best fit measured data. Due to ill-posedness issues, we use an iterative process finding at each step, a new $\boldsymbol{m}$ better fitting $\boldsymbol{d}$ **(**Fig. 1). The inverse problem can be formulated with the following expression:

$$\boldsymbol{m} = \mathfrak{F}^{-1}\boldsymbol{d} \qquad \text{(Eq. 3)}$$

The "best fit" of a given $\boldsymbol{d}$ depends on the definition of a cost function $\boldsymbol{\Gamma}$. The objective is to find $\boldsymbol{m}$ minimizing $\boldsymbol{\Gamma}$. Eq. 4 shows the definition $\boldsymbol{\Gamma}$ composed of an L2 norm on data ($\boldsymbol{\Gamma_d}$) and on the model ($\boldsymbol{\Gamma_m}$). $\boldsymbol{L}$ is a model smoothing matrix and $\boldsymbol{m_{ref}}$ is a reference model used to constrain the inversion (Constable, 1990). The damping factor λ enables a trade-off between the minimization of the data part of the cost function ($\boldsymbol{\Gamma_d}$) and the minimization of the model part of the cost function ($\boldsymbol{\Gamma_m}$) (Loke and Barker, 1996).

$$\boldsymbol{\Gamma} = \boldsymbol{\Gamma_d} + \lambda\boldsymbol{\Gamma_m} = \|\boldsymbol{d} - \mathfrak{F}(\boldsymbol{m})\|^{\boldsymbol{2}} + \lambda\left\|\boldsymbol{L}(\boldsymbol{m} - \boldsymbol{m_{ref}})\right\|^{\boldsymbol{2}} \qquad \text{(Eq. 4)}$$

Deriving eq. 4 leads to the normal equation of inversion (Loke and Barker, 1996). Eq. 5 is a compact formulation of the normal equation of inversion that can be efficiently solved with a QR decomposition method (Sasaki, 1994).

$$\begin{bmatrix}\boldsymbol{WJ}\\ \sqrt{\lambda}\boldsymbol{L}\end{bmatrix}\delta\boldsymbol{m} = \begin{bmatrix}\boldsymbol{W}(\boldsymbol{d} - \mathfrak{F}(\boldsymbol{m}))\\ \boldsymbol{m} - \boldsymbol{m_{ref}}\end{bmatrix} \quad \text{(Eq. 5)}$$

Where $\boldsymbol{\delta m}$ is the updating parameter vector, $\boldsymbol{W}$ is a data-weighting matrix and $\boldsymbol{J}$ is the sensitivity matrix, also known as the matrix of Fréchet derivates (Günther et al., 2006). $\boldsymbol{J}$ is computed with a perturbation method (Fares et al., 2016; McGillivray and Oldenburg, 1990). $\boldsymbol{L}$ is a positive definite diagonal matrix used to ensure the convergence of the inverse problem (Constable, 1990; Fares et al., 2016).

The inversion is an iterative process needing convergence criteria to be stopped. At each step, the iterative process finds a new model better fitting the measured data. Thus, the convergence criteria is the normalized root mean square error (*NRMSE*) between measured and calculated data (Loke and Barker, 1996).

For the numerical studies, we propose a similarity criterion E (%) giving a distance between the "inversed model" $\boldsymbol{\rho_{inv}}$ and the "true (synthetic) model" $\boldsymbol{\rho_{true}}$ (Eq. 6). To this end, each resistivity profile is discretized in p cells where $\boldsymbol{\rho_{inv}}$ and $\boldsymbol{\rho_{true}}$ are compared.

$$E = \sqrt{\frac{\sum_{i=1}^{p}\left(\frac{\rho_{true}-\rho_{inv}}{\rho_{inv}}\right)^2}{p}} \qquad \text{(Eq. 6)}$$

2.3 Inverse model parameterization

As previously mentioned, our aim is to retrieve *1D*-resistivity profiles with depth in cover concrete as reliably as possible. Thus, the inversion scheme developed here is *1D*, because it only focuses on resistivity variability with depth. We assume indeed that resistivity variations in other directions (parallel to the concrete surface) can be neglected (or averaged), at least at the scale of the used NDT device for our application.

The data in this study were measured on concrete slabs of finite dimensions (see section 4.1) (**Erreur ! Source du renvoi introuvable.**) thanks to a multi-electrode device developed by du Plooy et al. (2013). This *in situ* device is constituted of 14 aligned and equally spaced electrodes. Slab boundaries have a strong effect depending on slab dimensions, the electrode spacing and the position of the multi-electrode device on the slab (du Plooy et al., 2013). Due to the *3D* effects, we therefore implement a *3D* forward modelling of ρ_a data in our *1D*-inversion scheme. Note that the mesh is refined near the electrodes (Fig. 2). This allows to fully account for the actual geometry of the investigated slabs.

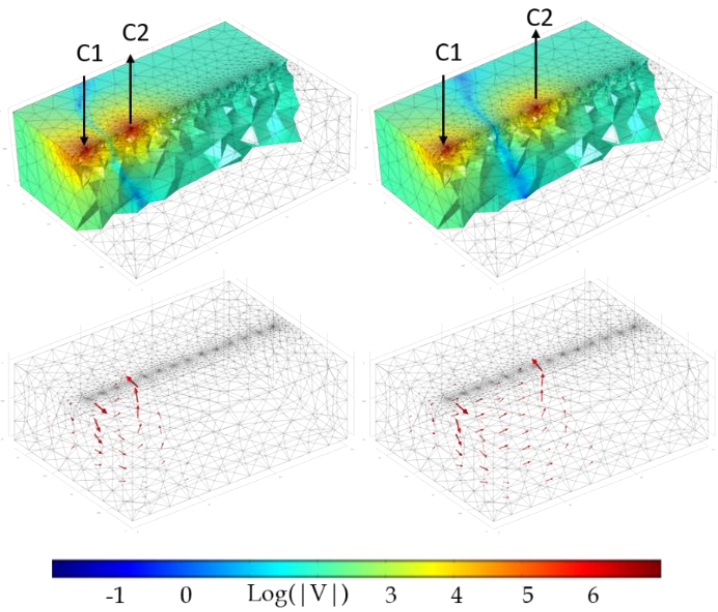

Fig. 2: Two numerical simulations of current flow between two electrodes C1 and C2 – a) Electrical potential distribution (V) for an inter-electrode spacing a=2 cm – b) Electrical potential distribution (V) for a=4 cm – c) Norm of the electrical current density for a=2 cm – d) Norm of the electrical current density for a=4 cm.

The way we perform the *1D* parametrization is of prime importance. Indeed, a trade-off must be found between a model with a high number of model parameters (potentially more representative of the medium) and the resolution capability of each model parameter in the inversion process. Indeed, a high number of model parameters leads to an under-determined problem and so to non-uniqueness issues. A low number of model parameters leads to an estimated model that is less representative of the true medium. Consequently, the objective is to find the model parameterization that is most representative of the "true" resistivity distribution while limiting at most the under-determination of the inverse problem.

We propose two parameterizations of the inverse model (Fig. 3). First, a discrete parameterization composed of three parameters (*3P*): One depth (z_1), and two resistivities (ρ_1, ρ_2). Second, a continuous parameterization based on the Weibull distribution composed of four parameters (*4P*) (Fares et al., 2016) (eq.7).

$$\rho(z) = (\rho_{sup} - \rho_{inf}) * \exp\left(-\left(\frac{z}{\tau}\right)^{k}\right) + \rho_{inf} \quad \text{(eq. 7)}$$

Where ρ_{sup} and ρ_{inf} are the asymptotic values of the medium resistivity (Ω. m) at surface and depth respectively. $\tau(mm)$ is the depth of the inflection point of the distribution. k is a shape parameter giving the stiffness of the distribution about its inflection point. Fig. 3 is a

schematic representation of the two models, with a perspective view of a) *3P* and d) *4P*, a longitudinal section of b) *3P* and e) *4P* and a *1D* plot of resistivity Vs depth of c) *3P* and f) *4P*.

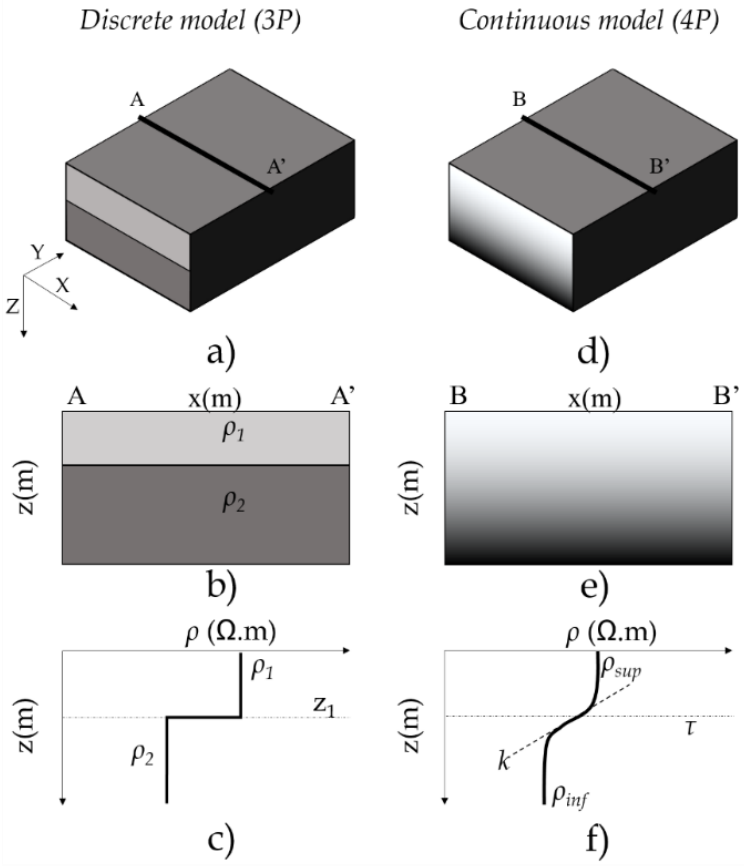

Fig. 3: Scheme of the two proposed parametrization models: discrete-*3P* and continuous-*4P* – a) Perspective view of *3P* - b) Longitudinal section of *3P* - c) Profile of resistivity versus depth of *3P* - d) Perspective view of *4P* - e) Longitudinal section of *4P* - f) Profile of resistivity versus depth of *4P*.

3 Numerical Study

This section presents a numerical study showing the benefits and drawbacks of the two parameterizations. To this end, we use various "true models" to compute synthetic measured data.

3.1 Model description

The modelling follows the characteristics of a real case study presented in section "experimental validation". Synthetic measurements are simulated on a slab (600*250*150 mm), whose resistivity profile is imposed by a true Weibull model (4 parameters, ρ_{sup}=500

Ω.m, ρ_{inf}=100 Ω.m, τ =30 mm and k=2). Fourteen electrodes assumed to be punctual are located at the centre of the upper surface of the slab. The acquisition protocol is a Wenner array (with 4 inter-electrode spacing a = 2, 4, 6, 8 cm) composed of 26 measurements.

3.2 Sensitivity study

We evaluate the two parameterizations by analizing the topology of the cost function $\boldsymbol{\Gamma_d}$ (Métivier and Brossier, 2016) in the model parameter space.

Firstly, the sensitivity of the continuous *4P*-parameterization is studied. To this end, $\boldsymbol{\Gamma_d}$ is computed for two fixed parametrers (fixed at their true value) and two variable ones among the four parameters (ρ_{sup}, ρ_{inf}, τ, k). Six variable pairs are studied more carefully (Fig. 4). Blue color shows the local minimum of the cost function with global minimum located at the red diamond ("true model"). Fig. 4 shows a non-convex objective function for four dual relations (Fig. 4b, c, e and f), comparable as a Rosenbrock's (1960) valley with a global minimum inside a long, narrow, parabolic shaped valley. As shown by Rosenbrock (1960), the valley is trivial to find. Conversely, finding the global minimum is harder (Fernández-Martínez et al., 2010). Moreover, the measurement error enhances the converging and non-uniqueness issues.

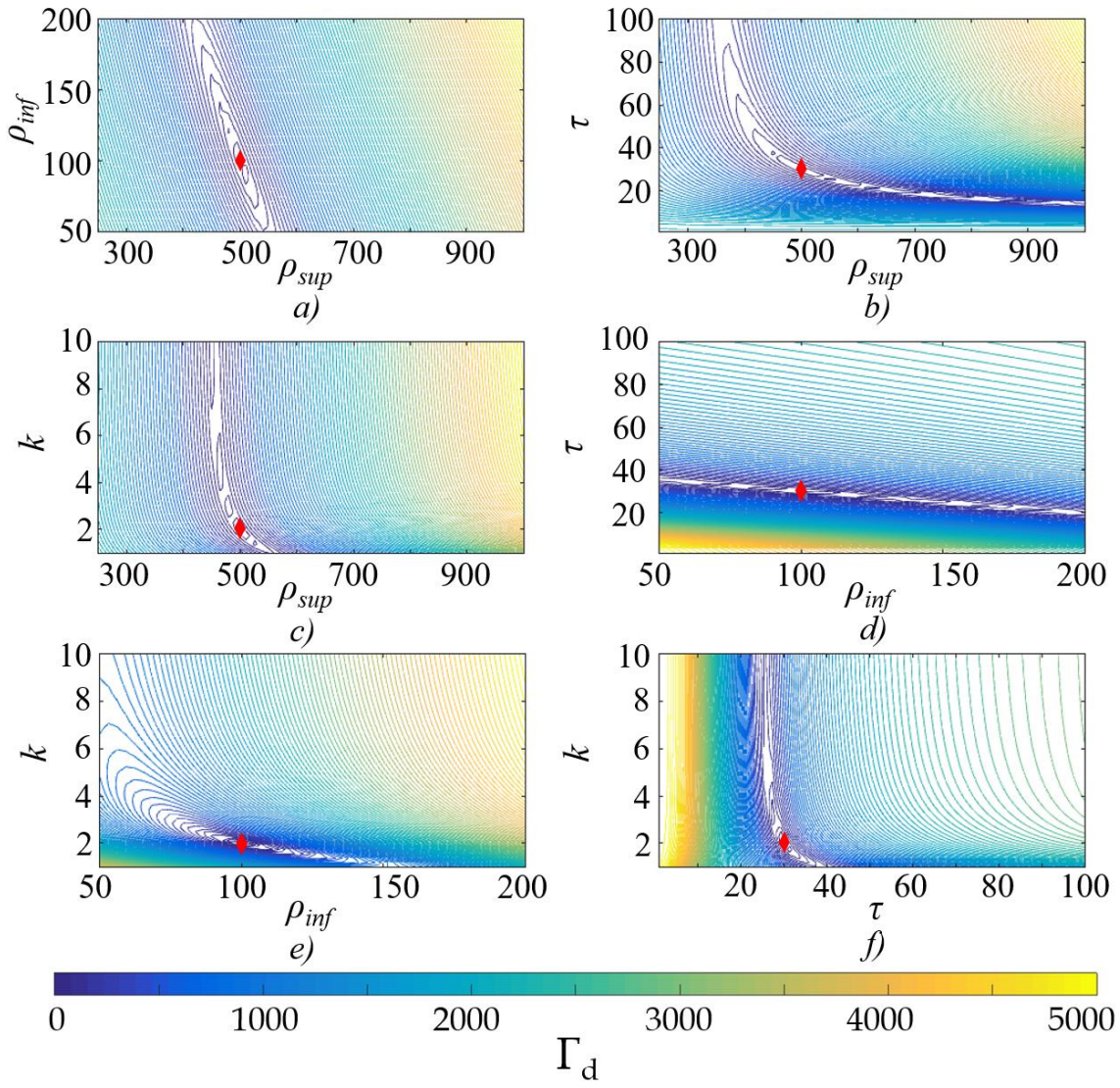

Fig. 4: Topology of Γ_d for six dual relations of the continuous 4P-model. a) ρ_{sup} Vs ρ_{inf}. b) k Vs ρ_{inf}. c) k Vs ρ_{inf}. d) τ Vs ρ_{sup} e) τ Vs ρ_{inf} and f) k Vs τ. Remaining model parameters set to true values. Red diamonds show the location of the true model.

Secondly, the sensitivity of the discrete *3P* parameterization is studied. The true model is that described in Section 3.1. The cost function $\mathbf{\Gamma_d}$ is computed for one fixed parametrers coresponding to its true value (i.e. ρ_1=500 Ω.m or ρ_2=100 Ω.m, or z_1 =30 mm) and the two remaining parameters as variables.

Fig. 5 shows the results of this study for the discrete *3P* parameterization. the true model (red diamond) is not located at the minimum of the cost function (blue region). Fig. 5.b and 5.c also show a non convex behaviour. This result is also interesting because it logically shows the inability of the *3P* parameterization to extract a smooth resistivity profile.

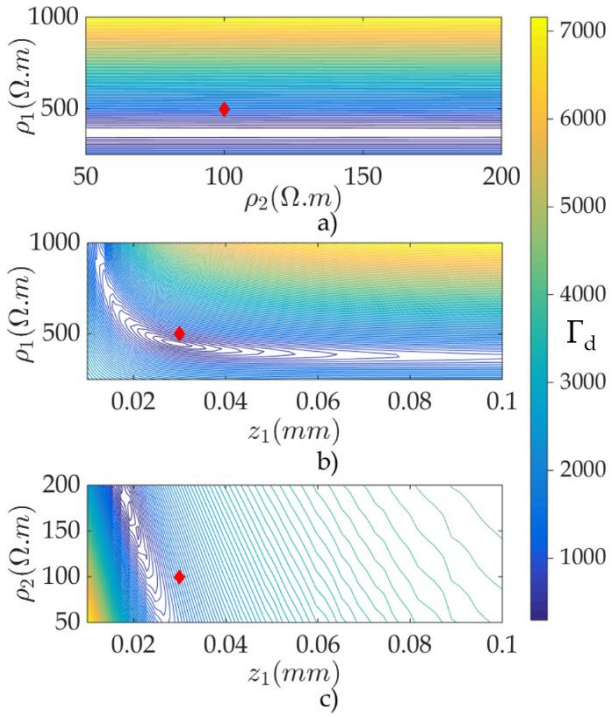

Fig. 5: Topology of the Γ_d contribution for three dual relations of the discrete *3P* discretization. Red diamonds show the location of the true model.

3.3 Numerical case study: comparison of continuous and discrete models

In this section we examine the benefits and drawbacks of the *4P* (continuous) and *3P* (discrete) parameterizations to extract resistivity profiles of realistic shape. To do that, three kinds of true models are imposed; they are based on the true model described in Section 3.1. For the first one, the parametre *k* is equal to 1 (*k*=1), which corresponds to a smooth profile of resistivity along depth that could be found in concrete with a low porosity (Villain and Thiery, 2006). Second and third models are a moderately steep (*k*=3) and steep (*k*=1000) profile respectively. Moreover, for the latter two models, various depths are evaluated (τ = 10, 20, 40 and 80 mm). The upper resistivity is always set to 500 Ω.m and lower resistivity is always set to 100 Ω.m.

Fig. 6 shows the inversion results of this study extracted at iteration 5. Concerning the smooth gradient (Fig. 6.a) and d)), the continuous parameterization accurately fits the true model while the discrete parameterization failed finding the 'true' solution.

Concerning the moderately steep (intermediate) gradient (Fig. 6.b) and e)), the interpretation is quite similar. The discrete *3P* parameterization fails to reconstruct the shape due to its parameterization. However, ρ_1, ρ_2 and z_1 are quite well extracted. The continous *4P* parametrization extracts accurately gradients at 20 and 40 mm. The shallower gradients

are quite well reconstructed with an error of 20 % on ρ_{sup}. The deeper gradient (80 mm) is not well reconstructed due to the loss of information with depth due to the multi-electrode device used in this study.

Concerning the steep gradient, the discrete model accurately inverts gradients located at 20 and 40 mm. For the resistivity profile located at 10 mm, ρ_1 is badly estimated. For the gradient at 5 mm, both ρ_1 and z are badly estimated. This discretization failed to extract the depth of the gradient at 80 mm and ρ_2. The continuous parameterization over-estimates ρ_{sup} for the two shallower gradients. This issue is due to the absence of information between 0 and 5 mm due to a too large inter-electrode spacing (2 cm) of the multi-electrode device. ρ_{inf} is well inversed because τ and z_1 are always lower than the theoretical depth of investigation. However, the model failed estimating the stiffness of the gradients below 5 mm depth. This issue increases when tau increases. This issue is linked oncemore with the sensitivity loss with depth that is intrinsic to the used multi-electrode device.

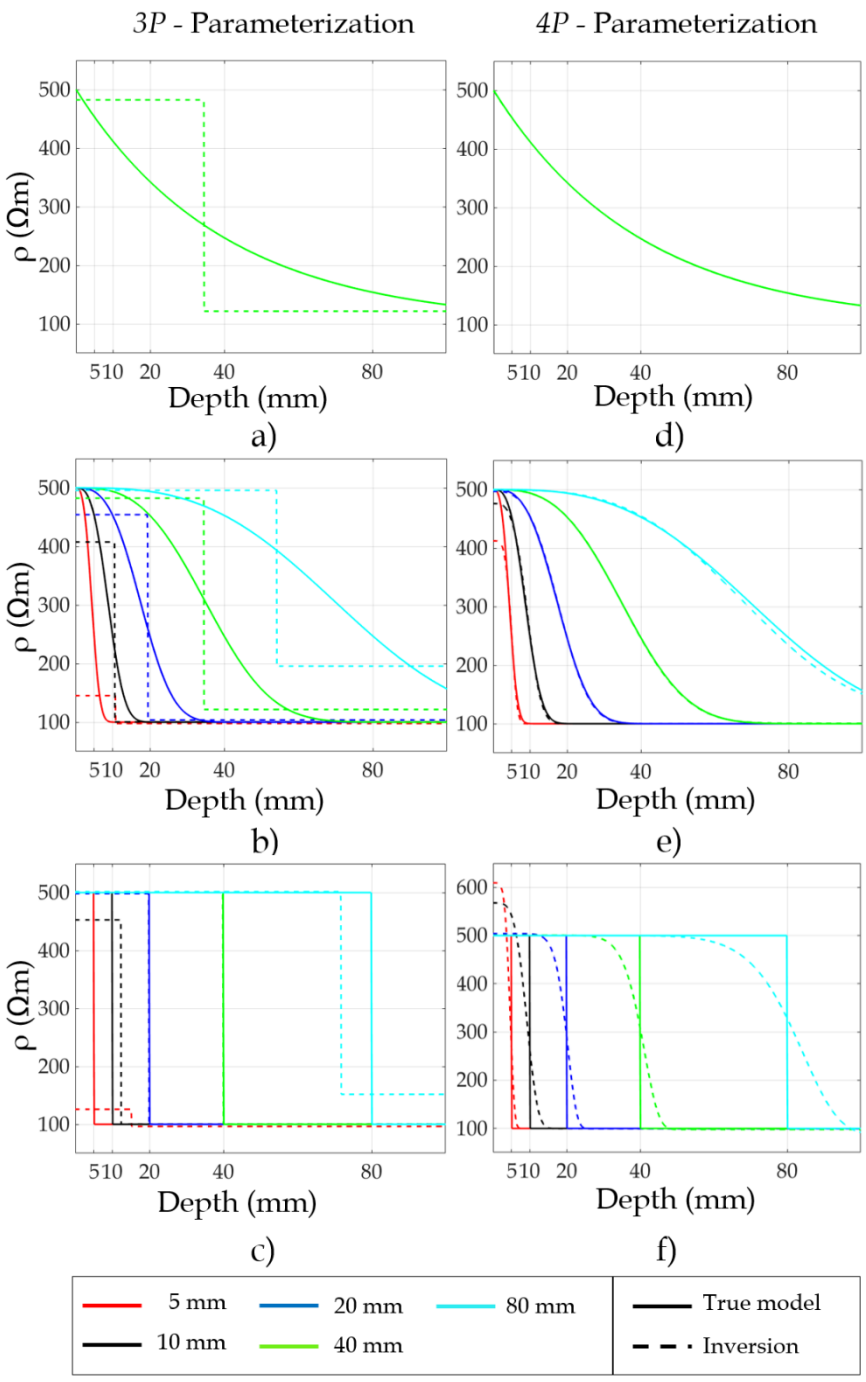

Fig. 6 : Synthesis of inversion results of synthetic measurements – a) Discrete inversion for the smooth profile – b) Continuous inversion for the smooth profile– c) Discrete inversion for the intermediate profiles – d) Continuous inversion for the intermediate profiles – e) Discrete inversion for the steep profiles – f) Continuous inversion for the steep profiles.

Table 1 synthetizes the results of the previous study. It gives the fitting error (*NRMSE*) and the similarity criterion (*E*). It shows that the continuous *4P* parameterization is better suited to fit relatively smooth resistivity profiles while the discrete *3P* parameterization is better suited to fit the steepest profiles except for very shallow profiles. It also shows that poor

results (high *E* value) are not always linked with a high *NRMSE* value due to the non-uniqueness of the solution.

Table 1: Inversion results of different "true model" obtained with the *3P* and *4P* models.

		Smooth profile		Intermediate profile		Steep profile	
Depth (mm)		*4P*	*3P*	*4P*	*3P*	*4P*	*3P*
5	*NRMSE (%)*	-	-	0	1.19	0.04	11.3
	E (%)	-	-	3.07	16.95	10.06	18.78
10	*NRMSE (%)*	-	-	0.01	0.09	0.04	0.38
	E (%)	-	-	1.55	11.83	15.86	16.29
20	*NRMSE (%)*	-	-	0.02	0.57	0.07	0.01
	E (%)	-	-	0.36	16.79	19.04	3.15
40	*NRMSE (%)*	0.02	1.04	0.03	0.56	0.04	2.01
	E (%)	0.2	20.41	0.49	24.79	27.68	1.88
80	*NRMSE (%)*	-	-	0.08	0.27	0.01	0.27
	E (%)	-	-	6.69	21.21	49.38	30.59

3.4 Numerical case study: effect of noise

We now examine the effect of the measurement noise on the inversion result. To this end, five noise levels are applied to the synthetic measured data (1, 2, 5, 10 and 20 %). The synthetic measured data are calculated with a true model corresponding to a moderately steep gradient with the following parameters : ρ_{sup} =500 Ω.m; ρ_{inf}= 100 Ω.m; τ = 20 mm; k= 6. The added noise is a Gaussian noise whose standard deviation is adapted to obtained the desired noise level (%). The new datasets are then inverted with the *3P* and *4P* parameterizations.

Fig. 7 shows the results of the inversions for three noise levels (I.E. 5%, 10% and 20%). 1% and 2% inversion results are not presented because the corresponding results cannot be distinguished from the "true model" for *4P*. For *3P* we cannot distinguish results 1% and 2% from the result at 5%. Fig. 7.a) shows that *4P* extracts well the resistivity profile even with 20 % of noise (cf. Table 2, E values). Concerning *3P*, interpretations of the results are similar to those shown in Fig. 6. The effect of the noise becomes important for the model at 10 % and 20 %. Below 5 % noise level, the inversion systematically yields the same profile.

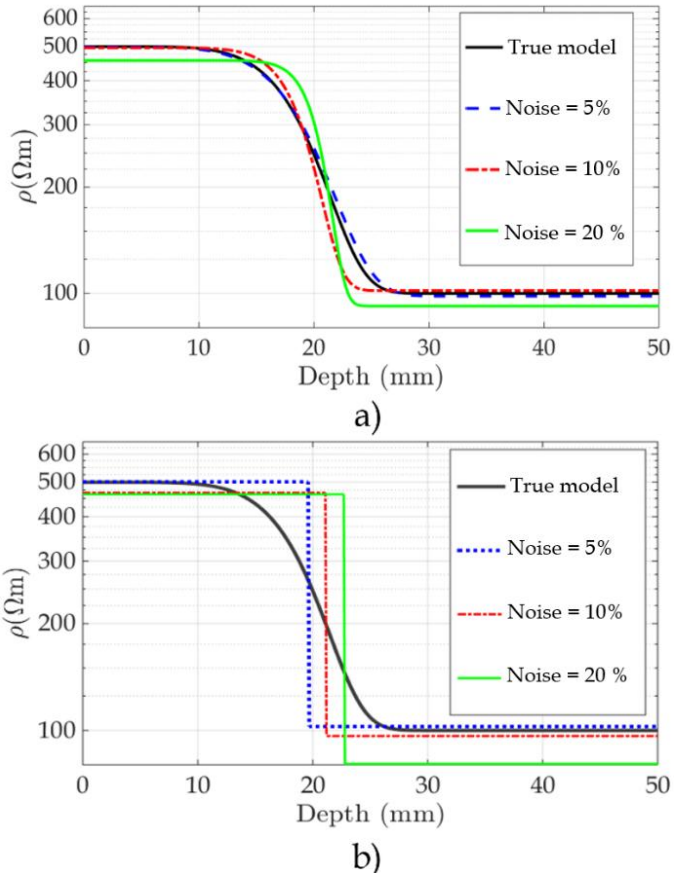

Fig. 7: Effect of three noise levels on the inversion – a) Continuous 4P parameterization – b) Discrete *3P* parameterization.

Table 2 synthetizes the inversion results. This table shows that the *NRMSE* values are very similar for the continous and discrete models and nearly equal to the noise level. Concerning the *E* criterion, it increases with the noise level for the continuous parametrization and remains quite similar for the discrete parameterisation for a noise level < 10 %. This difference between the *E* and *NRMSE* criteria can be interpreted as the effect of the non-uniqueness of the solution.

Table 2: Inversion results of synthetic data with an increasing noise level.

	Noise	Gaussian noise level (%)				
	Level	1	2	5	10	20
4P -continuous	ρ_{sup} (Ωm)	499.2	504.6	498.6	495.6	456.8
	ρ_{inf} (Ωm)	100.1	99.6	98.3	101.9	92.2
	τ (mm)	20.1	20.0	20.3	19.7	20.6
	k (-)	5.9	5.3	5.5	9.0	14.2
	E (%)	0.51	1.42	2.31	4.68	9.86
	NRMSE (%)	0.94	1.83	4.72	9.25	23.77
3P - discrete	ρ_1 (Ωm)	501.2	501.0	501.3	466.9	462.2
	ρ_2 (Ωm)	100.6	99.9	102.6	96.5	80.5
	z_1 (mm)	19.9	19.9	19.7	21.1	22.7

E (%)	14.28	14.52	13.92	17.13	32.20
NRMSE (%)	0.96	1.97	5.35	9.84	22.47

4 Experimental validation

The proposed inversion process of ρ_a datasets into true resistivity profiles is tested and validated on experimental measurements on concrete slabs submitted to water ingress to generate water content profiles. In a first step, the ρ_a measurements are inverted into resistivity profiles. In a second one, the resistivity profiles are converted into the profiles of saturation degree by using the calibration curve of the studied concrete. In a third step, the last profiles are compared to reference profiles of saturation degree obtained by gammadensimetry, which is classically used for this purpose (Villain and Thiery, 2006).

4.1 Concrete mix design and experimental program

The experimental campaign was led during a research project named ANR-EVADEOS (Balayssac et al., 2015; Villain et al., 2015a). The mix design (see Table 3) endows the C1 concrete a low compressive strength (21.5±1.0 MPa at 28 days) and a high porosity (18.3 ±0.3 %).

Table 3: Concrete mix design.

		Concrete C1
Aggregate type	round siliceous	D_{max} = 14 mm
Aggregate size 4-14	(kg/m^3)	1019
Sand 0-4	(kg/m^3)	941
Cement CEM I 52.5 N Calcia	(kg/m^3)	240
Total water	(kg/m^3)	193
Superplasticizer	(kg/m^3)	0.96
Water-to-cement ratio	*W/C(-)*	0.8

Three concrete slabs (600x250x150 mm) are devoted to the non-destructive testing campaign and other ones to coring. Four cores (∅75x70 mm) are used to build the conversion model of resistivity into saturation degree (i.e. the calibration curve). One core (∅100x150 mm) is used for gammadensimetry measurements. This semi-non-destructive method makes it possible to control the specimen conditions and to follow up the water penetration during the imbibition process. The profiles of saturation degree are obtained with an accuracy that is less than ±1 % in *S* and ±5 mm in depth (Villain and Thiery, 2006). Thus, gammadensimetry can be considered as a reference method in this paper. The three slab sides and the ∅ 100 core periphery are tight by two layers of adhesive aluminum foils to ensure unidirectional exchanges from their upper and lower faces.

Five thermohygrometric (THR) sensors per slab were embedded at five depths (15, 25, 40, 60 and 120 mm) at the end of each slab devoted to ND testing, to obtain the profile of relative humidity (*RH*) versus depth (Fig. 9). The ∅100 core, that follows the same experimental protocol as the three slabs, is tested by gammadensimetry at several test times during the imbibition campaign as well as in saturated conditions and dry conditions. For this core, the saturated state is obtained by water saturation under vacuum and the dry one by drying in an oven at 105°C until constant mass.

For the results presented here, all the specimens were submitted to pre-conditioning in an oven at T=45±5°C during seven days then wrapped in tight plastic bags and kept two months in the laboratory in order to obtain a homogeneous moisture distribution versus depth as much as possible.

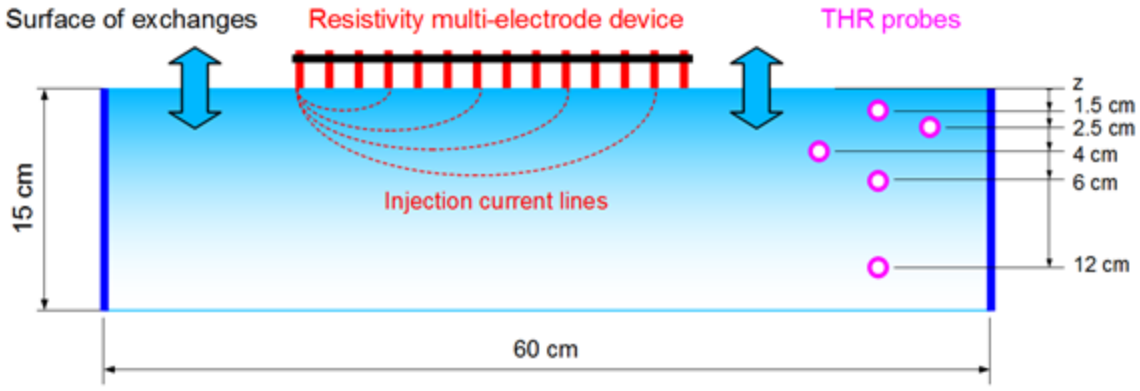

Fig. 8: Concrete slab water tight with aluminum foil and position of TRH probe and multi-electrode measurement device.

Just before the test time *t0*, TRH and gammadensimetry measurements were performed. At time *t0*, the slabs were immersed in 10 mm of water, in order to make water penetrate by an imbibition (or capillary absorption) process. At different test times, the slabs are taken out from water, the water excess is removed and multi-electrode measurements are performed on the humid upper face (Fig. 8). As soon as possible, the slabs are put back into water. The TRH are measured in the same time as the non-destructive testing. The ∅100 core follows a similar protocol for gammadensimetry.

As the slab surface was too dry to be able to use multi-electrode at *t0*, the first multi-electrode measurement was performed at *t0*+1/2h. The test times chosen for the comparison are *t0*+2h, *t0*+8h and *t0*+32h.

4.2 Calibration

Resistivity is influenced by the concrete formulation. Consequently, a conversion model (also called calibration curve) is needed to link the resistivity and the degree of saturation of the studied concrete. The calibration is performed in a resistivity cell developed by du Plooy et al. (2013). The protocol ensures that the sample is homogenous when considering its water content. Thus, it can be assumed that the cell evaluates the true effective resistivity of concrete ρ (du Plooy et al., 2013).

The protocol detailed in (Villain et al., 2015a) consists in a water saturation under vacuum, a partial homogeneous drying at three other targeted degree of saturation (here S_T=100%, 75%, 50%, 25%). At each step, the resistivity measurements are performed in the resistivity cell on the four cylindrical cores (∅75x70 mm) and they are weighted. After a complete drying at 105°C, the last weighing makes it possible to calculate the real degree of saturation S of the four samples at each test time. The results are the calibration curve and the conversion models of S versus ρ and ρ versus S (Fig. 9).

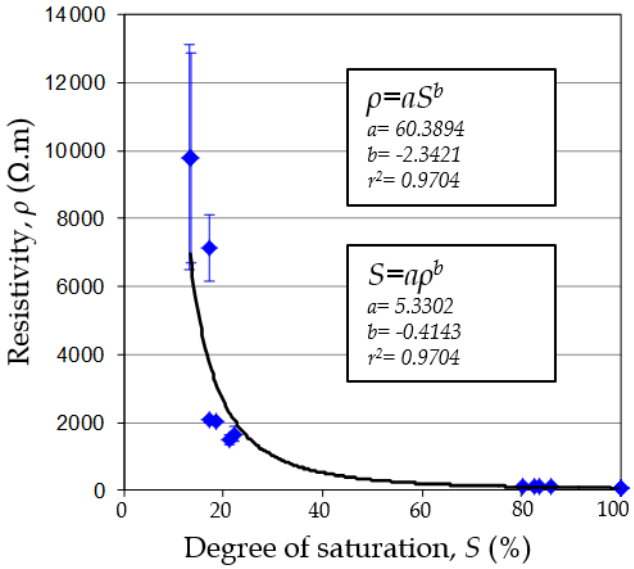

Fig. 9: Calibration curve of the studied concrete and conversion model of resistivity into degree of saturation.

4.3 Integrated raw measurements

At each test-time, ρ_a measurements were performed on three close locations on each slab: one in the middle of the wet upper face, another one shifted from the center 1 cm to one edge of the slab and the last one shifted 1 cm to the other edge.

Fig. 10.a presents the raw measurement results obtained for the three slabs for an electrode spacing equal to 4 cm (level 2). It shows the good reproducibility of the measurements, which is also the case for all levels at all test-times except for level 1 at *t0*+1/2h.

Fig. 10.b shows the temporal evolution of the mean values for four pseudo-depth levels. At *t0*+1/2h, the shallower apparent resistivity (ρ_{app1}) is higher than the others ($\rho_{app1} > \rho_{app2} > \rho_{app3} > \rho_{app4}$) which means that the slab is more humid at core than it is at the surface. The slabs are not homogeneously dried. Then, during the imbibition process, the water penetrates from the surface in contact with water, where the multi-electrode measurements are performed. So the apparent resistivities ρ_{app1} for the first level drop drastically whereas the decrease is slower for the other levels. This means that the water ingress can be monitored by the multi-electrode method.

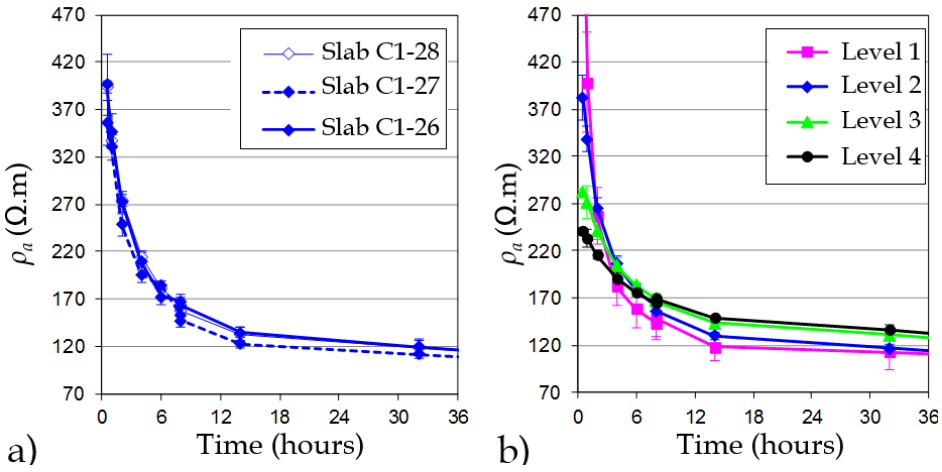

Fig. 10: Evolution of apparent resistivity along time during the imbibition process – a) Reproducibility of ρ_{app2} at level 2 (a = 4 cm) – b) Mean values on the three slabs.

4.4 Analysis of inverted profiles

The ρ_a were inverted at four test-times (at *t0*+1/2h, *t0*+2h, *t0*+8h and *t0*+32h) by using the discrete *3P* (Fig. 11.a) and the continuous *4P* parameterizations (Fig. 11.b). These 'true' resistivity profiles show the water ingress effect. The discrete *1D* profile seems unable to correctly locate the waterfront. The continuous Weibull profiles have to be converted into degree of saturation to be compared to reference profiles.

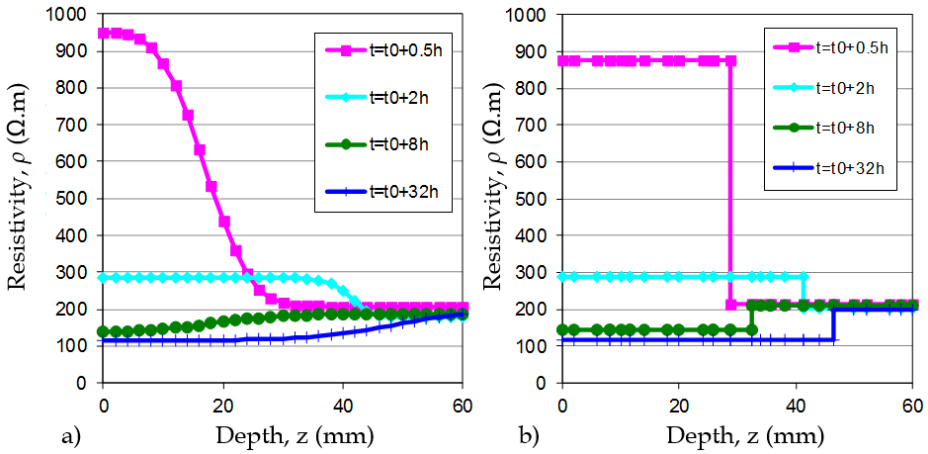

Fig. 11: Inversion results of true resistivity profiles in slab C1-28 – a) Continuous *3P* parameterization – b) Discrete *4P* parameterization.

The conversion model presented above (Fig. 8) makes it possible to compare the profiles obtained by gammadensimetry and those obtained by the multi-electrode device (Fig. 12.a). At the first test-time, the profiles obtained by both methods show that the slab is more humid at core than at its surface. Nevertheless, the degree of saturation evaluated by the multi-electrode device is lower ($S \approx 31\%$) than S evaluated by gammadensimetry ($S \approx 45\%$). This can be explained by the measurement technique. The 1-cm gamma-ray beam is indeed centered at $z = 8$ mm, so it cannot investigate the first three millimeters and the 4^{th} millimeter is of less influence. Conversely, for the multi-electrode device, the first four millimeters of the subsurface have the greatest influence.

At *t0*+2h, the position of the waterfront is correctly evaluated. However, the inversion process, that assumes a monotonous profile by using the 4P parameterization, falls to describe this non-monotonous profile. Concerning the test-times *t0*+8h and *t0*+32h, the profiles obtained by both methods agree well. To better highlight this agreement, the variations of saturation degree were calculated (*S-S(t0)* for gamma but *S-S(t0+1/2h)* for the multi-electrode device). These variations can be observed in **Erreur ! Source du renvoi introuvable.**.

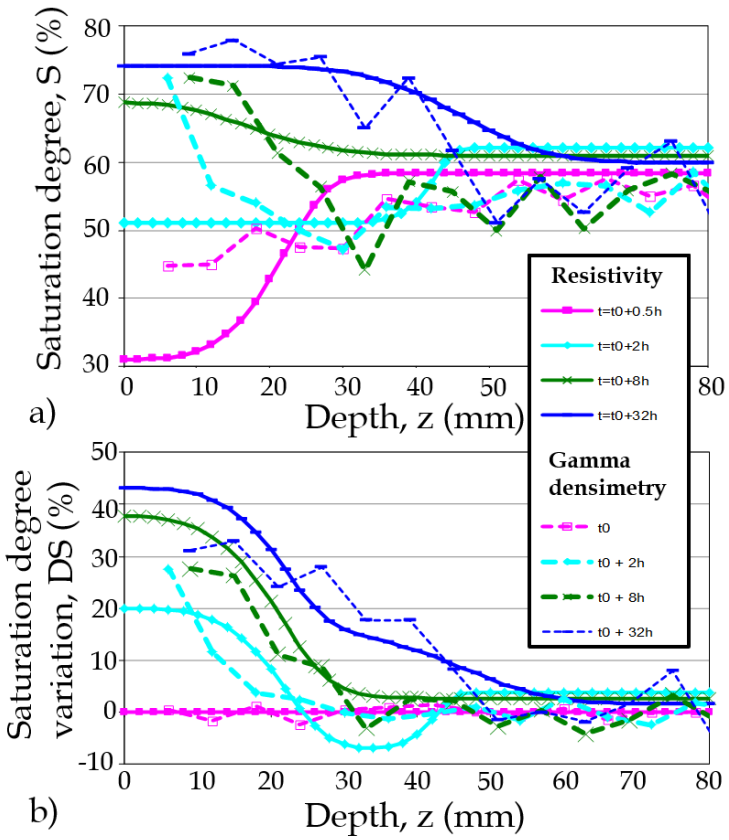

Fig. 12: Profiles obtained by the resistivity (*4P*) (slab C1-28) and gammadensimetry methods (C1 cylindrical sample) – a) Profiles of saturation degree – b) Profiles of the saturation degree variations.

5 Discussion

This paper aims to demonstrate that one can retrieve resistivity profiles vs. depth within cover concrete by implementing a *1D* inversion scheme based on i) a *3D* forward modelling fully accounting for the geometry of a given case, ii) a smoothness constrained least squares algorithm for effectively fitting the model parameters and iii) the use of model parameterizations that implicitely introduce a priori information on the expected profile shapes. The latter item was developed in order to yield an optimal model parameterization by comparing a discrete one based on two layers (*3P*) and a continuous one based on a Weibull distribution (*4P*). The numerical study illustrates the effiency of our *1D* inversion approach, even when up to 20 % gaussian noise is added to the synthetic data. It also points out advantages and drawbacks of each parameterization strategy and shows that the continuous *4P* distribution clearly stands out, except when the resistivity profile exhibits a very steep gradient which might only be the case of extremely porous concrete. Moreover, our approach is applied to real data from an experimental programme in which high-porosity concrete slabs

were exposed to water imbibition and monitored by means of the multi-electrode acquisition device at specific times after the imbibition start. Results obtained with the continuous *4P* parameterization prove superior, as they better fit the real data. These results are compared to gammadensimetry measurements which provide a finer resolution whith depth than for the resistivity measure. These independently measured saturation degree profiles exhibit oscillations with depth (due to differences in density between coarse agregates and paste). Therefore our inverted results, which are monotonous by definition, can only match the general trend of the profiles measured on cores by gammadensimetry. However, the resemblance is significantly better when comparing the saturation degree variations from the first test timewith depth, because the initial state of the specimens is not homogeneous but, nevertheless, has to be taken as the onset of the imbibition process. We think that a continuous parameterization that intrinsincally mimics the expected shape of saturation degree profiles in cover concrete (a priori information) is a powerful tool for quantitatively and reliably retrieving useful information on water ingress (very useful information for monitoring applications).

6 Conclusion

The aim of this paper was to introduce a methodology that is based on an innovative NDE technique when applied to cover concrete assessment. The methodology allows the retrieval of *1D* resistivity profiles versus depth in cover concrete to better characterize the water ingress phenomenon. The innovative side concerns the optimized parametrization of the inverse problem in function of our a priori knowledge on the medium. In order to show the feasibility of our *1D* profile extraction approach, two parameterization schemes were presented, believed to be relevant for the demonstration and for such applications. The first parameterization strategy is a discrete 3-parameters (*3P*) model (to describe sharp front constituted of two contrasted layers) while the second is a continuous 4-parameters (*4P*) model based on a Weibull function (to describe monotous water content gradients). Both strategies were tested numerically and a sensitivity study shows the relative influence of each model parameter. The two parameterization approaches were compared on synthetic cases exhibiting very smooth to very steep resistivity profiles. The discrete *3P* parameterization only shows better results for the very steep resistivity profile (e.g. a very sharp water front in cover concrete). The continuous *4P* parameterization proves more efficient for fitting smooth to moderately steep resistivity profiles and shows great potential even when up to 10 %

gaussian noise is added to data. Future research includes testing other parameterization and inversion schemes as well as enhancing data acquisition design and taking the effect of steel reinforcement into account. We also esteem that a generalisation of these specially designed parametrization could benefits in numerous field applications and more especialy when the data is scarse or noisy and our a priori on the model is strong.

Acknowledgements

The authors wish to thank the French Ministry for an Ecological and Solidary Transition and the research project SENSO for the funding. Authors thanks more particularly Odile Coffec and Jean-Luc Geffard for their assistance for the measurement campaign.

References

Archie, G.E., 1942. The electrical resistivity logs as an aid in determining some reservoir characteristics 146, 54–62.

Badr, J., Fargier, Y., Palma-Lopes, S., Deby, F., Balayssac, J.-P., Delepine-Lesoille, S., Cottineau, L.-M., Villain, G., 2019. Design and validation of a multi-electrode embedded sensor to monitor resistivity profiles over depth in concrete. Constr. Build. Mater. 223, 310–321.

Balayssac, J.-P., Garnier, V., Villain, G., Sbartaï, Z.-M., Dérobert, X., Piwakowski, B., Breysse, D., Salin, J., 2015. An overview of 15 years of French collaborative projects for the characterization of concrete properties by combining NDT methods. In: Proceedings of Int. Symp. on NDT-CE. pp. 15–17.

Baroghel-Bouny, V. et al., 2007. Concrete Design for a Given Structure Service Life: Durability Management with Regard to Reinforcement Corrosion and Alkali-silica Reaction : State of the Art and Guide for the Implementation of a Predictive Performance Approach Based Upon Durability Indicators, Documents scientifiques et techniques. AFGC.

Bentur, A., Diamond, S., Berke, N.S., 1997. Steel Corrosion in Concrete – Fundamentals and Civil Engineering Practice, E & FN SPON. ed. London, United Kingdom.

Constable, de G.-H., 1990. Occam's inversion to generate smooth, two-dimensional models from magnetotelluric data 55, 1613.

Dérobert, X., Iaquinta, J., Klysz, G., Balayssac, J.-P., 2008. Use of capacitive and GPR techniques for the non-destructive evaluation of cover concrete. NDT E Int. 41, 44–52.

du Plooy, R., Palma Lopes, S., Villain, G., Dérobert, X., 2013. Development of a multi-ring resistivity cell and multi-electrode resistivity probe for investigation of cover concrete condition. NDT E Int. 54, 27–36.

du Plooy, R., Villain, G., Lopes, S.P., Ihamouten, A., Dérobert, X., Thauvin, B., 2015. Electromagnetic non-destructive evaluation techniques for the monitoring of water and chloride ingress into concrete: a comparative study. Mater. Struct. 48, 369–386.

Fares, M., Fargier, Y., Villain, G., Derobert, X., Lopes, S.P., 2016. Determining the permittivity profile inside reinforced concrete using capacitive probes. NDT E Int. 79, 150–161.

Fargier, Y., Antoine, R., Dore, L., Lopes, S., Fauchard, C., 2017. 3D assessment of an underground mine pillar by combination of photogrammetric and geoelectric methods. Geophysics 82, E143–E153.

Fargier, Y., Lopes, S.P., Fauchard, C., François, D., Côte, P., 2014. DC-Electrical Resistivity Imaging for embankment dike investigation: A 3D extended normalisation approach. J. Appl. Geophys. 103, 245–256.

Fernández-Martínez, J.L., García-Gonzalo, E., Naudet, V., 2010. Particle swarm optimization applied to solving and appraising the streaming-potential inverse problem. Geophysics 75, WA3–WA15.

Gowers, K.R., Millard, S.G., 1999. Measurement of Concrete Resistivity for Assessment of Corrosion Severity of Steel Using Wenner Technique. Mater. J. 96, 536–541.

Günther, T., Rücker, C., Spitzer, K., 2006. Three-dimensional modelling and inversion of dc resistivity data incorporating topography - II. Inversion 166, 506–517.

Holcombe, H.T., Jiracek, G.R., 1984. Three-dimensional terrain corrections in resistivity surveys 49, 439–452.

Hugenschmidt, J., Loser, R., 2007. Detection of chlorides and moisture in concrete structures with ground penetrating radar. Mater. Struct. 41, 785–792.

Ihamouten, A., Chahine, K., Baltazart, V., Villain, G., Derobert, X., 2011. On variants of the frequency power law for the electromagnetic characterization of hydraulic concrete 60, 3658–3668.

Karhunen, K., Seppänen, A., Lehikoinen, A., Monteiro, P.J., Kaipio, J.P., 2010. Electrical resistance tomography imaging of concrete. Cem. Concr. Res. 40, 137–145.

Kwon, S.-J., Feng, M.Q., Park, S.S., 2010. Characterization of electromagnetic properties for durability performance and saturation in hardened cement mortar. NDT E Int. 43, 86–95.

Lataste, J.F., Behloul, M., Breysse, D., 2008. Characterisation of fibres distribution in a steel fibre reinforced concrete with electrical resistivity measurements. NDT E Int. 41, 638–647.

Loke, M., Chambers, J., Rucker, D., Kuras, O., Wilkinson, P., 2013. Recent developments in the direct-current geoelectrical imaging method 95, 135–156.

Loke, M.H., Barker, R.D., 1996. Rapid least-squares inversion of apparent resistivity pseudosections by a quasi-Newton method1 44, 131–152.

McGillivray, P.R., Oldenburg, D.W., 1990. Methods for Calculating Frechet Derivatives and Sensitivities for the Non-Linear Inverse Problem: a Comparative STUDY1. Geophys. Prospect. 38, 499–524.

Métivier, L., Brossier, R., 2016. The SEISCOPE optimization toolbox: A large-scale nonlinear optimization library based on reverse communication. Geophysics.

Monfore, G.E., 1968. The electrical resistivity of concrete. Portland Cem. Assoc R Lab Bull.

Polder, R.B., 2001. Test methods for on site measurement of resistivity of concrete — a RILEM TC-154 technical recommendation. Constr. Build. Mater., Near Surface Testing of 15, 125–131.

Pridmore, D.F., Hohmann, G.W., Ward, S.H., Sill, W.R., 1981. An investigation of finite-element modeling for electrical and electromagnetic data in 3 Dimensions 46, 1009–1024.

Reichling, K., Raupach, M., Klitzsch, N., 2015. Determination of the distribution of electrical resistivity in reinforced concrete structures using electrical resistivity tomography. Mater. Corros. 66, 763–771.

Rosenbrock, H.H., 1960. An Automatic Method for Finding the Greatest or Least Value of a Function. Comput. J. 3, 175–184.

Rücker, C., Günther, T., Spitzer, K., 2006. Three-dimensional modelling and inversion of dc resistivity data incorporating topography - I. Modelling. Geophys. J. Int. 166, 495–505.

Sasaki, Y., 1994. 3-D resistivity inversion using the finite-element method 59, 1839–1848.

Sbartai, Z.M., Laurens, S., Rhazi, J., Balayssac, J.P., Arliguie, G., 2007. Using radar direct wave for concrete condition assessment: Correlation with electrical resistivity 62, 361–374.

Spitzer K., 2007. A 3- D finite- difference algorithm for DC resistivity modelling using conjugate gradient methods. Geophys. J. Int. 123, 903–914.

Tarantola, A., Valette, B., 1982. Inverse problems= quest for information. J Geophys 50, 150–170.

Villain, G., Garnier, V., Sbartaï, Z.M., Dérobert, X., Balayssac, J.-P., 2018. Development of a calibration methodology to improve the on-site non-destructive evaluation of concrete durability indicators. Mater. Struct. 51.

Villain, G., Ihamouten, A., du Plooy, R., Lopes, S.P., Dérobert, X., 2015a. Use of electromagnetic non-destructive techniques for monitoring water and chloride ingress into concrete. Surf. Geophys. 13, 299–309.

Villain, G., Sbartai, Z.M., Lataste, J.F., Garnier, V., Dérobert, X., Abraham, O., Bonnet, S., Balayssac, J.P., Nguyen, N.T., Fares, M., 2015b. Characterization of water gradients in concrete by complementary NDT methods, International Symposium on Non Destructive Testing in Civil Engineering. Presented at the Internation Symposium on Non Destructive Testing in Civil Engineering (NDT-CE 2015), Berlin, Germany, pp. 448–459.

Villain, G., Thiery, M., 2006. Gammadensimetry: A method to determine drying and carbonation profiles in concrete. NDT E Int. 39, 328–337.

Whittington, H.W., McCarter, J., Forde, M.C., 1981. The conduction of electricity through concrete. Mag. Concr. Res. 33, 48–60.

Woelfl, G.A., Lauer, K., 1979. The Electrical Resistivity of Concrete with Emphasis on the Use of Electrical Resistance for Measuring Moisture Content. Cem. Concr. Aggreg. 1, 64–67.

Zohdy, A., 1989. A new method for the automatic interpretation of Schlumberger and Wenner sounding curves. GEOPHYSICS 54, 245–253.